Reconstruction of fission events in heavy ion reactions with the compact spectrometer for heavy ion experiment

Xin-Yue Diao[1] · Fen-Hai Guan[1] · Yi-Jie Wang[1] · Yu-Hao Qin[1] ·
Zhi Qin[1] · Dong Guo[1] · Qiang-Hua Wu[1] · Da-Wei Si[1] · Xuan Zhao[1] ·
Sheng Xiao[1] · Yao-Peng Zhang[1] · Xiang-Lun Wei[2] · Hai-Chuan Zou[3] ·
He-Run Yang[2] · Peng Ma[2] · Rong-Jiang Hu[2] · Li-Min Duan[2] · Artur Dobrowolski[4] ·
Krzysztof Pomorski[4] · Zhi-Gang Xiao[1]

Abstract We report a reconstruction method for fast-fission events in 25 MeV/u ^{86}Kr + ^{208}Pb reactions at the Compact Spectrometer for Heavy Ion Experiment (CSHINE). The fission fragments (FFs) are measured using three large-area parallel-plate avalanche counters, which can deliver the position and arrival timing information of the fragments. The start timing information is provided by the radio frequency of the cyclotron. Fission events were reconstructed using the velocities of the two FFs. The broadening of both the velocity distribution and azimuthal difference of the FFs decreases with the folding angle, in accordance with the picture that fast fission occurs. The anisotropic angular distribution of the fission axis also consistently reveals the dynamic features of fission events.

Keywords Fast fission · Heavy ion reactions · Parallel-plate avalanche counter · CSHINE

✉ Xin-Yue Diao
dxy17@mails.tsinghua.edu.cn

[1] Department of Physics, Tsinghua University, Beijing 100084, China

[2] Institute of Modern Physics, Chinese Academy of Sciences, Lanzhou 730000, China

[3] School of Nuclear Science and Technology, Lanzhou University, Lanzhou 730000, China

[4] Institute of Physics, Maria Curie Skłodowska University, Lublin 20031, Poland

1 Introduction

One of the purposes of studying heavy ion reactions (HIRs) is to infer the properties of the nuclear equation of state, which is an essential input for modeling and computing the evolution and properties of neutron stars and their merging [1–3]. The isovector sector of the nuclear equation of state, namely, the density behavior of the symmetry energy $E_{sym}(\rho)$, has been a long-standing open question in nuclear physics. At Fermi energies, some observables have been identified to constrain $E_{sym}(\rho)$ near normal density, including isospin diffusion, dipole polarizability, and particle emissions [4–10]. Very recently, neutron skin thickness has been reported from the PREX II experiment, which yields a stiff $E_{sym}(\rho)$ in relation to previously existing constraints [11, 12]. At supra-saturation densities, many experiments have been conducted to measure the charged pion ratios or collective flow in heavy-ion collisions to probe $E_{sym}(\rho)$ [13, 14]. An external-target experiment (the Heavy Ion Research Facility in Lanzhou CSR External-target Experiment) is under construction in this direction [15, 16].

Nuclear fission is a large-amplitude collective motion mode that involves hundreds of nucleons. Recently, studies on nuclear fission have been revived for their significance in both nuclear physics and astrophysics. In a stellar environment, the abundance of nuclides in the $A \approx 160$ region is significantly influenced by the recycling of fission products [17–19]. Theoretically, statistical fission has been well described by microscopic theories and various phenomenological approaches [20–32]. When the excitation energy or angular momentum becomes much higher, as achieved in HIRs well above the Coulomb barrier, the fission barrier tends to vanish. Consequently, the fission

time scale becomes shorter by a factor of 10–100, and the variance of the mass asymmetry η increases significantly (where η of the two fragments can be >0.6), compared to that of statistical fission [33–37]. In this case, the dynamic feature of the fission process is significant, and transport models have been successfully applied to describe the fast-fission process [38–46]. Time-dependent Hartree–Fock theory can also provide an excellent description of fast fission, starting with large deformations [47]. Fast fission, which is usually termed dynamic fission because of its vanishing fission barrier and short time scale, has been investigated in various systems in the past three decades [48–54].

The topic of fast fission with simultaneous emission of light particles deserves further investigation because the fissioning system provides an appropriate laboratory for probing $E_{sym}(\rho)$. The connection between the studies of fast fission and $E_{sym}(\rho)$ has recently been established by simulations with improved quantum molecular dynamics (ImQMD) [55, 56]. It has been suggested that the fast-fission process following an HIR carries the effect of $E_{sym}(\rho)$ and provides sensitive probes because of the formation of a low-density and neutron-rich neck and the larger surface of two fragments compared to the non-fission process [56, 57]. The isospin content of light particles emitted from fast-fission events has been used to probe $E_{sym}(\rho)$ experimentally [10].

To conduct experimental studies on fast fission and coincident emission of light charged particles (LCPs) and intermediate-mass fragments (IMFs), the Compact Spectrometer for Heavy Ion Experiment (CSHINE) has been developed [58, 59]. While the LCPs and IMFs are measured using silicon strip detector telescopes (SSDTs) [60, 61], the fission fragments (FFs) are measured using parallel-plate avalanche counters (PPACs) [62].

In this study, we present the measurement of fast fission in $^{86}Kr + {}^{208}Pb$ reactions with CSHINE in the second phase. After a brief introduction to the phase-II setup of CSHINE in Sect. 2, the reconstruction of the FF velocity is introduced in Sect. 3, and the dynamic features of fast fission are presented in Sect. 4. Section 5 provides a summary of this study.

2 CSHINE detector system and the experimental setup

The beam experiment was conducted on Radioactive Ion Beam Line I (RIBLL1) at the Heavy Ion Research Facility in Lanzhou, China. The ^{208}Pb target with an areal density of 1 mg/cm^2 was bombarded with a 25 MeV/u ^{86}Kr beam. The charged reaction products were measured using CSHINE, which was installed in a large scattering chamber located at the final focal plane of RIBLL1. In this experiment, three PPACs were installed for FF measurements to reconstruct the reaction geometry. In addition, four SSDTs were installed for LCPs covering the polar angle range of $10° < \theta_{lab} < 60°$. The SSDTs are three-layer detectors with a single-sided SSD for ΔE_1 as layer 1, a double-sided SSD for ΔE_2 as layer 2, and a 3×3 CsI (Tl) array for residual energy measurements as layer 3. Both single- and double-sided SSDs are BB7 types (with a 2 mm strip width and 32 strips on each side) from Micron Semiconductor Ltd. Each CsI (Tl) crystal is a square pyramid with dimensions of 23×23 mm^2 on the front side, 27×27 mm^2 on the rear side, and 50 mm in height. A photodiode (Hamamatsu S3204) was used to read out the signal from the CsI. Fig. 1 presents the detector setup of CSHINE in the experiment that can measure FFs and coincident LCPs simultaneously. Details and performance of CSHINE can be found in [58, 59]. Table 1 presents the distance d from the center of each detector to the target, polar angle θ, azimuthal angle ϕ, and sensitive area S of the SSDTs and PPACs in the experiment. The thicknesses of ΔE_1 and ΔE_2 for each SSDT are also listed.

The FF detector (PPAC) is a type of multiwire chamber working in the region of limited proportionality. The signals induced by the incident fragments on an individual wire in the anode plane, either X or Y, were transferred through a delay line to both ends. The time delay of the two signals X_1 and X_2 (Y_1 and Y_2) with respect to the signal collected on the cathode plane, which delivers the timing information, provides the X (Y) position of the hit in the sensitive area. Fig. 2 presents a schematic view of the mechanics of the PPAC. The total thickness of the sensitive gas layer was ~ 2 cm. The PPACs were operated with 4.5 mbar isobutane at a voltage of 465 V. Under this condition, FFs can be recorded with an efficiency of >95%, but the LCPs and IMFs are suppressed.

Figure 3b shows a two-dimensional histogram of $Y_1 - Y_2$ versus $X_1 - X_2$ for PPAC1 as an example. The projections to X and Y directions are plotted in Fig. 3a and c,
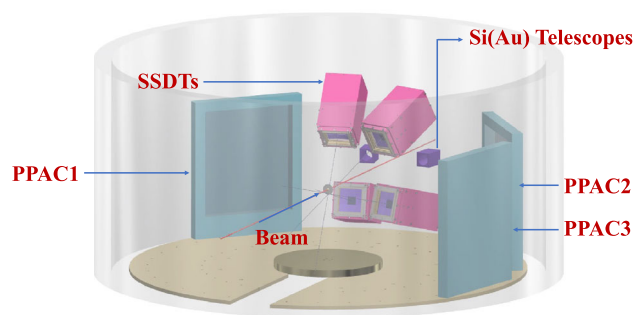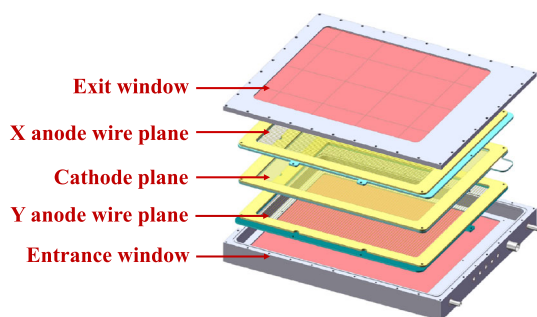

Fig. 1 (Color online) Schematic view of CSHINE phase II

Table 1 Geometric parameters of PPACs and SSDTs

Detector	d (mm)	θ (°)	ϕ (°)	S (mm²)	ΔE_1 (μm)	ΔE_2 (μm)
SSDT1	315.5	18	302	64×64	304	1010
SSDT2	275.5	25	218	64×64	305	1008
SSDT3	275.5	31	126	64×64	110	526
SSDT4	215.5	51	81	64×64	70	306
PPAC1	427.5	50	0	240×280	–	–
PPAC2	427.5	55	180	240×280	–	–
PPAC3	427.5	100	180	240×280	–	–

Fig. 2 (Color online) Schematic view of PPAC as the FF detector
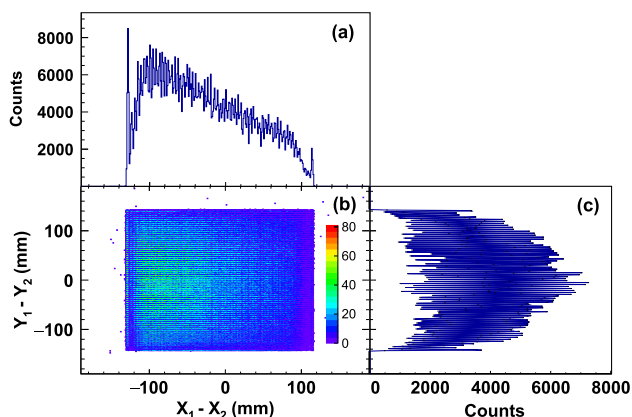
Fig. 3 (Color online) Scattering plots of $Y_1 - Y_2$ versus $X_1 - X_2$ of PPAC1. Panels **a** and **c** show the projections of the two-dimensional plot of $X–Y$ in panel **b**

respectively. Good timing performance, corresponding to good position resolution, manifests itself in the sharp boundary for the two-dimensional distribution and the well-separated individual peaks on the projections. The distance of the neighboring wires is 4 mm, and there are 61 and 71 peaks in Fig. 3a and c, respectively. A time resolution of $\sigma_T = 300$ ps and a position resolution of $\sigma_r = 1.35$ mm can be derived from the data. The overall performance of the PPACs can be found in [62].

The SSDTs were used to measure the LCPs and IMFs in coincidence with the FFs. To reduce the total number of electronic components, every two neighboring strips were merged into one channel, and correspondingly, the

granularity was reduced. Multi-tracks can fire each SSDT. To reconstruct the tracks in the SSDTs, a novel algorithm was developed with a special focus on the charging sharing effect. More than 80% of the hits in all layers of the SSDTs can be recognized and assigned to certain tracks. For more details, refer to [60].

The CSHINE trigger system was designed for both the beam experiment and calibration. The timing signals of PPACs were discriminated by a Constant-Fraction Discriminator CF8000 and logically calculated using a Quad 4-Input Logic Units CO4020 to generate PPAC inclusive signals and PPAC two-body coincidence signals. The logic hit signals of the SSDTs were extracted by the front side of the double-sided SSD (ΔE_2) with the discrimination of MSCF-16, which generates an analog multitrigger signal proportional to the number of fired strips in the same module (16 channels). Both inclusive and exclusive logic signals can be generated by discriminating multi-trigger signals at different threshold settings. In the beam experiment, the trigger signal contained SSD two-body events, PPAC two-body events, and the coincidence of PPAC two-body with SSD one-body events. In addition, an inclusive trigger for every individual detector was also constructed and optionally turned on for detector calibration before or after beam data acquisition. For more details, refer to [60].

3 Reconstruction of the velocity

We concentrated on the reconstruction of fission events. The flight path of FFs can be determined by PPACs delivering good position information. The velocity of each FF is derived from the timing information. In previous experiments, because the absolute flight time of fragments was not measured, we could obtain only the difference of flight time between fragments. Therefore, we could not directly obtain the velocity of the fragments [63, 64]. It is notable that the starting time information was recorded in this experiment provided by the radio frequency (RF) of the accelerator. The RF signal, usually in sinusoidal form, was discriminated by the CF8000 module and input to the

time-to-digital converter (TDC). Generally, for a particle firing a given detector, the time of flight (*TOF*) is written as

$$TOF = t_{\text{det}} - t_{\text{RF}} - C_{\text{det}}, \qquad (1)$$

where t_{det} and t_{RF} are the time signals of the detector and the RF, respectively, recorded by the corresponding TDC channels, and C_{det} is a constant representing a fixed delay in electronics, the matching of the RF signal, and so on. The units of both time signals were calibrated in nanoseconds using a precise time calibrator. The velocity was then computed as

$$v = \frac{L}{TOF}, \qquad (2)$$

where *L* is the length of the flight path from the target to the hit position where the fragment fires on the detector.

To verify the validity of the above method for measuring the *TOF*, we use calibrated α particles, where the velocity is alternatively derived from the energy measured in SSDT3. Fig. 4a presents the correlation between the α energy and the *TOF* derived by Eq. (1). The theoretical curve fitting of the *E*–*TOF* profile applies a constant $C_{\text{det}} = 431.8$ ns. Fig. 4b presents the difference between the *TOF* measured by the TDC and the value $L/v(E_\alpha)$, where *v* is derived from the energy E_α and *L* is the distance from the target to the hit position in SSDT3. A width of 1.3 ns is obtained by Gaussian fitting. By subtracting the contribution of the energy uncertainty, a *TOF* resolution of ∼1.0 ns was obtained for the SSDT. For the FF measured in PPACs, the *TOF* resolution is comparable because the timing resolution of PPACs is 300 ps, which is much better than that of the SSDT.

With the validity of Eq. (1), we can discuss the *TOF* of the FFs. Because PPACs cannot identify the charge or mass of the FFs, nor the total kinetic energy, one relies on the determination of the velocities, which requires *TOF* information and the length of the flight path, *L*. In Eq. (1),

the relative difference in the delay constants, $C_{\text{ppac1}} - C_{\text{ppac2}}$, between the two PPACs can be adjusted to zero using a pulser prior to the experiment, and the systematic uncertainty can be well controlled within ±2 ns. However, the absolute value of C_{ppac} of each PPAC cannot be determined, as in the SSDT, because the particle type and total energy are unknown. To overcome this difficulty, we use Viola systematics in which the relative velocity of the FFs is on average 2.4 cm/ns [65]. Hence, by tuning the constant C_{ppac}, one can optimize the value of $<v_{\text{FF}}> = 2.4$ cm/ns. Figure 5 presents the distribution of v_{FF} values at different delay constants. It can be observed that the peak position of v_{FF} moves significantly by varying the delay constant by 2 ns. In our experiment, $C_{\text{ppac}} = 115.5$ ns was optimized, and the corresponding distribution of v_{FF} values is plotted in Fig. 5b. The variation of $<v_{\text{FF}}>$ is 0.1 cm/ns based on transport model calculations and a 2 ns systematic uncertainty of the *TOF* of FFs is estimated, which will not change the conclusion of the following analysis. We recall that the coincident events recorded by PPAC1 with PPAC2 (marked by PPAC1 × 2) or with PPAC3 (marked by PPAC1 × 3) are the FFs because the high voltage (HV) condition is set such that the response of PPAC to energetic LCPs and IMFs is completely suppressed, given that the energy loss of these particles is less than that of FFs by more than an order of magnitude. In addition, the correlation between a heavy projectile-like fragment and a target-like fragment (TLF) is beyond the current geometrical coverage.
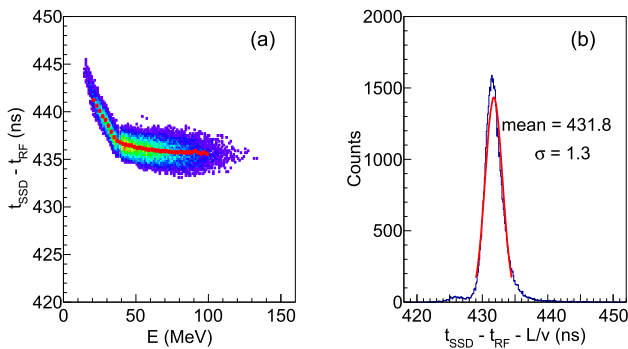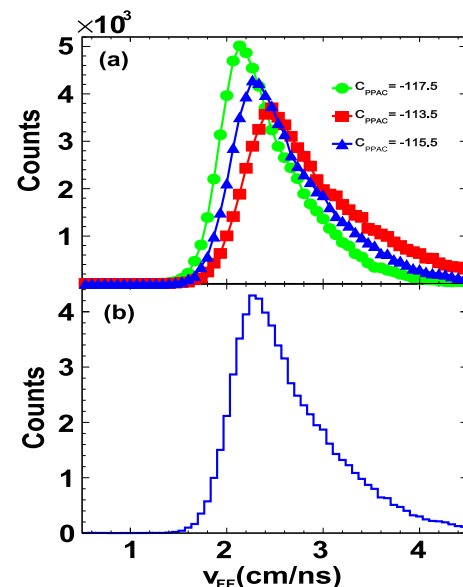

Fig. 4 (Color online) **a** Correlation of the *TOF* signal and the energy of α particles recorded by SSDT3. **b** Distribution of the time difference between the TDC measurement and the calculated value from the calibrated energy

Fig. 5 (Color online) Relative velocity distribution v_{FF} of the two FFs with different parameter settings of C_{PPAC}

4 Results and discussion

Before discussing the reconstruction of fission events, we first define the fission kinetics. In incomplete fusion, a heavy TLF is formed in the fusion of a part of the projectile and the target. The fraction of momentum of the projectile transferred to the TLF is called the linear momentum transfer (LMT). With a certain probability, depending on the total angular momentum of the reaction system, the TLF may undergo fission or fast fission in competition with the emission residue channel. Figure 6 presents the kinetic geometry of the TLF fission event. The origin point O is the target nucleus in the laboratory system and the vector OO' represents the direction of the beam. The velocity vectors $\mathbf{v}_{f_1}$ and $\mathbf{v}_{f_2}$ of the two FFs in the laboratory system are represented by OA and OB. $\mathbf{v}_{tl}$ is the velocity of the TLF, and the velocities of the two fragments in the center-of-mass system of the fissioning TLF are represented by $\mathbf{v}'_{f_1}$ and $\mathbf{v}'_{f_2}$, sitting back to back collinearly. Here, we define plane OAB as the fission plane, plane $OO'A$ as the projection plane, and plane DOO' as the reaction plane.

Once *TOF* is determined, the velocity of the FFs can be computed event by event using the hit positions of the FFs in the PPACs. Subsequently, the entire fission event can be reconstructed. Figure 7 presents the velocity distributions of the FFs in PPAC1 × 2 and PPAC1 × 3 events, respectively. Here, $\mathbf{v}_{f_1}$ is the FF recorded in PPAC1 and $\mathbf{v}_{f_2}$ is the FF in PPAC2 (PPAC3) in PPAC1 × 2 (PPAC1 × 3) events. The figure shows that the distributions of $\mathbf{v}_{f_1}$ and $\mathbf{v}_{f_2}$ are very similar for PPAC1 × 2 events, because the two PPACs are nearly symmetric with respect to the beam. Meanwhile, a high-velocity tail is evident in PPAC1 × 2 events, and the velocity spectra are wider than those in PPAC1 × 3 events. This component is mainly due to events with smaller folding angles, corresponding to larger LMTs, as will be discussed below.

After the velocities of the two FFs are determined, the folding angle method is applied to calculate the LMT of the reaction. By recalling the definitions in Fig. 6, the folding angle Θ_{FF} is defined as the angle $\angle AOC$, spanned by the projection of the velocity vectors of the FFs on the
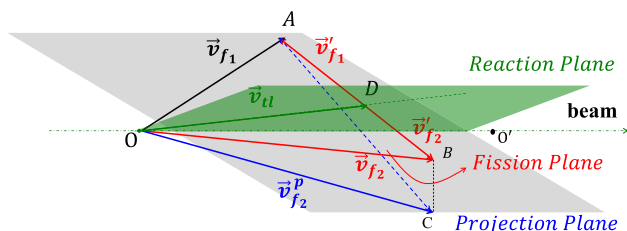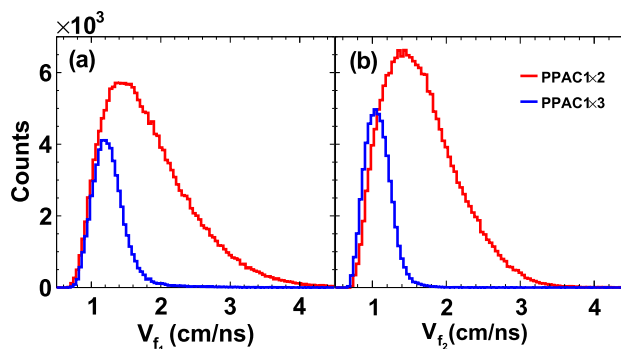

Fig. 7 (Color online) Velocity distribution of the two FFs in PPAC1 × 2 and PPAC1 × 3 events

projection plane [66]. Given velocities $\mathbf{v}_{f_1}$ and $\mathbf{v}_{f_2}$, the folding angle depends on the velocity of the TLF, $\mathbf{v}_{tl}$; that is, the larger the value of $\mathbf{v}_{tl}$, the smaller Θ_{FF} will be. Figure 8 presents the distribution of the folding angle Θ_{FF}. The coincident events of PPAC1 × 2 are distributed in the range of $70° − 120°$ with a peak situated at $\sim 95°$, corresponding to a larger LMT (red), whereas the PPAC1 × 3 events sit in the range of $120°–170°$, corresponding to a smaller LMT (blue). The valley between the two components is simply due to the deficiency caused by the gap between PPAC2 and PPAC3, and the efficiency arising from incomplete azimuthal coverage is not corrected in the plot.

As the fission geometry is determined by the two velocity vectors, it is of interest to examine the planarity of fission events. Figure 9a presents the azimuth correlation of the two FFs by a scattering plot between the azimuthal angle difference $\Delta\phi$ and the folding angle Θ_{FF}. It is clear that, for the FFs from both central and peripheral reactions, the most probable value is $\Delta\phi = 180°$, following the situation in which the system undergoes a binary decay. Here, we note that $\Delta\phi$ is a directly measurable quantity that relies on no assumptions. The inset shows the projection distribution of $\Delta\phi$, and a standard deviation of $\sigma(\Delta\phi) \approx 10°$ was derived. This broadening suggests that the emission of LCPs or IMFs may change the flight direction of the FF
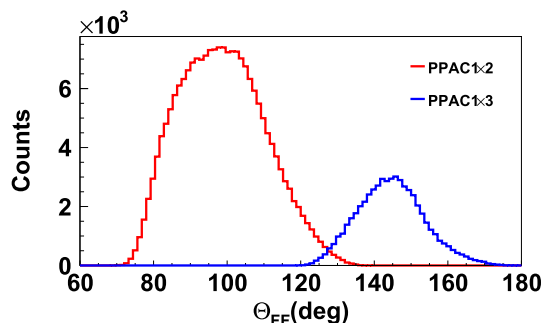

Fig. 6 (Color online) Geometric diagram of the velocities of the two FFs from the TLF

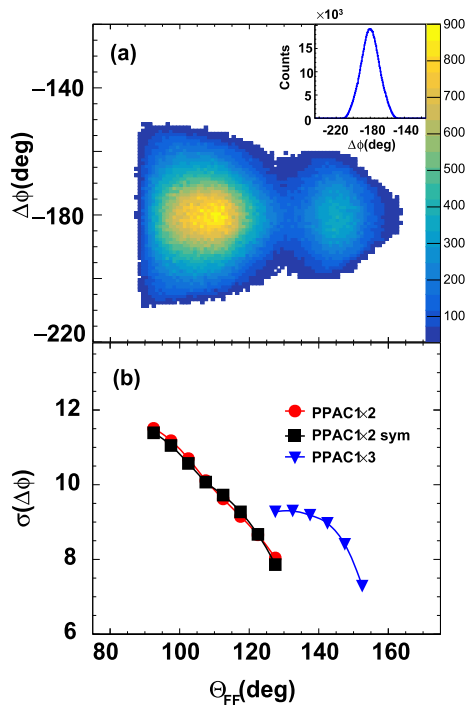**Fig. 8** (Color online) Folding angle distribution

Fig. 9 (Color online) **a** Azimuthal angle difference $\Delta\phi$ as a function of the folding angle Θ_{FF} of the FFs. The inset shows the projection distribution of $\Delta\phi$. **b** $\sigma(\Delta\phi)$ as a function of Θ_{FF}

and smear the back-to-back feature of the fission event. To investigate its evolution with the violence of the reaction, we plotted in Fig. 9b the standard deviation of the azimuthal angle, $\sigma(\Delta\phi)$, as a function of the folding angle Θ_{FF}. The figure shows that $\sigma(\Delta\phi)$ decreases with Θ_{FF} over the entire range, except for $\Theta_{FF} \approx 130°$, where a discontinuity appears owing to the gap between PPAC2 and PPAC3. To exclude the possible reason that this trend originates from the asymmetry of the geometrical locations of the PPACs, we restrict further analysis of the events with the two FFs flying symmetrically in the beam direction, that is, with the condition of $\theta_1 = \theta_2$, where θ_i is the polar angle of the ith fragment. The results are depicted by black squares, where the bin width of each Θ_{FF} is $\pm 2.5°$. This condition is applicable only for PPAC1 $\times$ 2 fission events because these two PPACs are placed in an approximate left–right symmetry with respect to the beam line. It is evident that the data points with the symmetry condition are sitting on top of those without the condition, suggesting that the decreasing trend of $\sigma(\Delta\phi)$ as a function of Θ_{FF} is truly due to reaction violence. Because the post-scission particle emission changes the velocity of the FF owing to the recoil effect, the trend suggests that, in the fission following the intermediate-energy HIRs, there is sufficient excitation energy left at the scission point depending on the LMT. In the reactions with a larger LMT, more excitation energy is left and released through particle emission in the

post-scission stage. This is consistent with fast fission, instead of statistical fission in which the excitation energy is nearly depleted at the scission point.

The dynamic features of fast fission can be further explored based on the velocity distribution of the FFs. Figure 10a presents the average of the velocities of the FFs recorded in the PPACs as a function of folding angle. From Fig. 10a, one can observe that the average velocity value $<v_f>$ decreases with the folding angle. Figure 10b presents the standard deviation of the velocity, $\sigma(v_f)$. It is also clear that the broadening of the velocity of the FFs decreases with the folding angle. This result is consistent with the trend in $\sigma(\Delta\phi)$ in Fig. 9. The scission point is reached early when the excitation energy of the fissioning TLF is still high; thus, the statistical fluctuation (corresponding to the left excitation energy) enhances the variance in the velocity of the FF. This is consistent with earlier experimental observations of Ar + ^{209}Bi reactions at 25 MeV/u [67–69].

Finally, the dynamic features of fast fission may also cause anisotropy in the angular distribution of the fission axis. Here, the fission axis is defined as the vector of the relative velocity, $\mathbf{v}_{FF}$, from f_2 to f_1, where f_1 and f_2 are fragments. Λ_{FF} is the angle of the fission axis with respect to the beam axis as defined in [55]. Usually, the experimental measurement of the distribution of Λ_{FF} requires fine correction of the geometric efficiency; hence, it is more feasible to use a 4π detection system.

In our experiment, PPACs cover only part of the entire space, and we fix the direction of the first FF in PPAC1 to introduce less ambiguity to the geometry efficiency correction. In this case, we only need to correct the efficiency
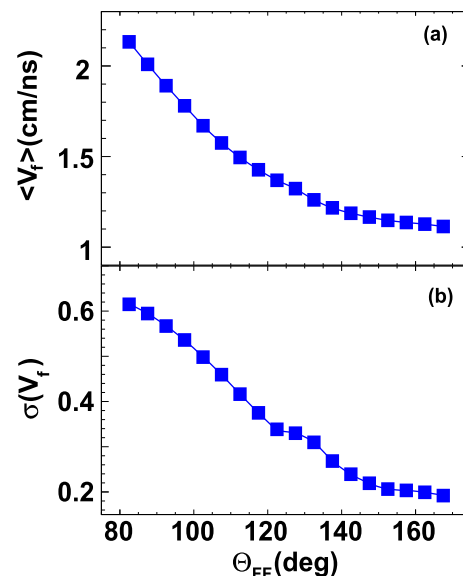

Fig. 10 (Color online) **a** Average value of velocity and **b** standard deviation of the velocity distribution as a function of folding angle

of the second FF on PPAC2 and PPAC3, and the trend of the angular fission axis can be inferred. Figure 11 presents correlation plots of the parallel and transverse velocities of the FFs. Here, the transverse velocity of the FFs recorded in PPAC1 is defined as positive and that in the other two PPACs is defined as negative. It is clear that there was a dead area of $20°$ between PPAC2 and PPAC3. The dashed lines define a narrow range of $40° < \theta_{f_1} < 45°$, which was fixed in the investigation of the distribution properties of the fission axis as described in the following.

The distribution of $d\sigma/d\cos(\Lambda_{FF})$ is shown in Fig. 12. The geometric efficiency arising from the incomplete azimuth coverage of PPAC2 and PPAC3 is corrected for each Λ_{FF} bin. The events of PPAC1 $\times$ 2 and PPAC1 $\times$ 3 are represented by symbols, whereas the curve represents the sum. The figure clearly shows that the deficiency in the gap between PPAC2 and PPAC3 causes a kink in a wide range of $63° < \Lambda_{FF} < 80°$. Regardless of the kink area and the uncovered region within $\Lambda_{FF} < 50°$, the distribution of $dN/d\cos(\Lambda_{FF})$ increases steadily with $\cos(\Lambda_{FF})$ and tends to peak at a forward angle, which is at variance with the expectation of an isotropic distribution for statistical fission. This trend is in qualitative agreement with previously reported experimental results for HIRs at Fermi energies [48, 49].

5 Summary

In summary, FFs in 25 MeV/u ^{86}Kr + ^{208}Pb reactions were measured using the CSHINE detection system. In the current phase, three PPACs and four SSDTs were mounted to measure the FFs and coincident LCPs and IMFs, respectively. Using the timing and position signals of the PPACs and the start timing from the RF of the accelerator, we can measure the velocities of the FFs and reconstruct
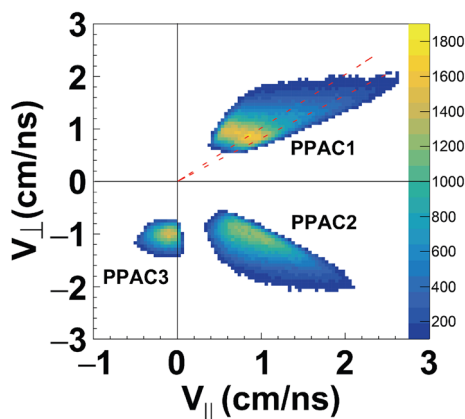

Fig. 11 (Color online) Transverse and parallel velocity distribution of the FFs
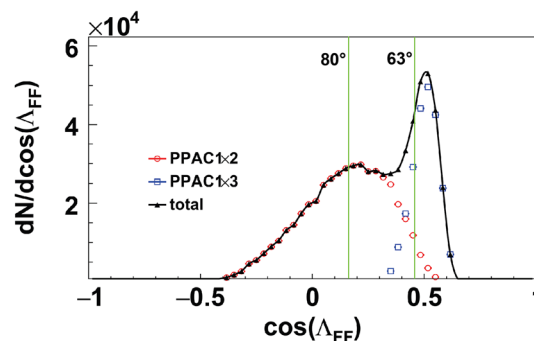

Fig. 12 (Color online) Angular distribution $dN/d\cos(\Lambda_{FF})$ of the fission axis with respect to the beam

the fission events, where LMT can be derived from the folding angle. It is shown that the width of the azimuthal angle difference, the mean value, and the width of the velocity distribution of the FFs all decrease with the folding angle. An anisotropic angular distribution of the fission axis is observed. These results are consistent with the situation in which fast fission occurs. Prospectively, with the ability of reconstructing the fission events, CSHINE provides opportunities to study isospin dynamics and nuclear symmetry energy by further counting the coincident isotope-resolved LCPs and IMFs.

References

1. B.A. Li, B.J. Cai, W.J. Xie et al., Progress in constraining nuclear symmetry energy using neutron star observables since GW170817. Universe **7**, 182 (2021). https://doi.org/10.3390/universe7060182
2. B.P. Abbott, R. Abbott, T.D. Abbott et al., GW170817: Observation of gravitational waves from a binary neutron star inspiral. Phys. Rev. Lett. **119**, 161101 (2017). https://doi.org/10.1103/PhysRevLett.119.161101
3. B.P. Abbott, R. Abbott, T.D. Abbott et al., GW170817: Measurements of neutron star radii and equation of state. Phys. Rev. Lett. **121**, 161101 (2018). https://doi.org/10.1103/PhysRevLett.121.161101
4. M.B. Tsang, T.X. Liu, L. Shi et al., Isospin diffusion and the nuclear symmetry energy in heavy ion reactions. Phys. Rev. Lett. **92**, 062701 (2004). https://doi.org/10.1103/PhysRevLett.92.062701
5. L.W. Chen, C.M. Ko, B.A. Li, Determination of the stiffness of the nuclear symmetry energy from isospin diffusion. Phys. Rev. Lett. **94**, 032701 (2005). https://doi.org/10.1103/PhysRevLett.94.032701
6. M.B. Tsang, W.A. Friedman, C.K. Gelbke et al., Isotopic scaling in nuclear reactions. Phys. Rev. Lett. **86**, 5023–5026, 032701 (2001). https://doi.org/10.1103/PhysRevLett.86.5023
7. L.W. Chen, C.M. Ko, B.A. Li et al., Density slope of the nuclear symmetry energy from the neutron skin thickness of heavy

nuclei. Phys. Rev. C **82**, 024321 (2010). https://doi.org/10.1103/PhysRevC.82.024321

8. Z. Zhang, L.W. Chen, Constraining the density slope of nuclear symmetry energy at subsaturation densities using electric dipole polarizability in ^{208}Pb. Phys. Rev. C **90**, 064317 (2014). https://doi.org/10.1103/PhysRevC.90.064317

9. M.B. Tsang, Y.X. Zhang, P. Danielewicz et al., Constraints on the density dependence of the symmetry energy. Phys. Rev. Lett. **102**, 122701 (2009). https://doi.org/10.1103/PhysRevLett.102.122701

10. Y. Zhang, J.L. Tian, W.J. Cheng et al., Long-time drift of the isospin degree of freedom in heavy ion collisions. Phys. Rev. C **95**, 041602 (2017). https://doi.org/10.1103/PhysRevC.95.041602

11. D. Adhikari, H. Albataineh, D. Androic et al., Accurate determination of the neutron skin thickness of through parity-violation in electron scattering. Phys. Rev. Lett. **126**, 172502 (2021). https://doi.org/10.1103/PhysRevLett.126.172502

12. B.T. Reed, F.J. Fattoyev, C.J. Horowitz et al., Implications of PREX-2 on the equation of state of neutron-rich matter. Phys. Rev. Lett. **126**, 172503 (2021). https://doi.org/10.1103/PhysRevLett.126.172503

13. J. Estee, W.G. Lynch, C.Y. Tsang et al., Probing the symmetry energy with the spectral pion ratio. Phys. Rev. Lett. **126**, 162701 (2021). https://doi.org/10.1103/PhysRevLett.126.162701

14. Y.J. Wang, Q.F. Li, Application of microscopic transport model in the study of nuclear equation of state from heavy ion collisions at intermediate energies. Front. Phys. **15**, 44302, 162701 (2020). https://doi.org/10.1007/s11467-020-0964-6

15. L.M. Lü, H. Yi, Z.G. Xiao et al., Conceptual design of the HIRFL-CSR external-target experiment. Sci. China-Phys. Mech. Astron. **60**, 012021 (2016). https://doi.org/10.1007/s11433-016-0342-x

16. L.M. Lü, H. Yi, L.M. Duan et al., Simulation and prototype testing of multi-wire drift chamber arrays for the CEE. Nucl. Sci. Tech. **31**, 11, 012021 (2020). https://doi.org/10.1007/s41365-019-0716-x

17. G. Lorusso, S. Nishimura, Z.Y. Xu et al., β-decay half-lives of 110 neutron-rich nuclei across the $n = 82$ shell gap: Implications for the mechanism and universality of the astrophysical r process. Phys. Rev. Lett. **114**, 192501 (2015). https://doi.org/10.1103/PhysRevLett.114.192501

18. N. Nishimura, T. Kajino, G.J. Mathews et al., Impact of new β-decay half-lives on r-process nucleosynthesis. Phys. Rev. C **85**, 048801 (2012). https://doi.org/10.1103/PhysRevC.85.048801

19. T. Suzuki, T. Yoshida, T. Kajino et al., β decays of isotones with neutron magic number of $n = 126$ and r-process nucleosynthesis. Phys. Rev. C **85**, 015802 (2012). https://doi.org/10.1103/PhysRevC.85.015802

20. K. Pomorski, J. Bartel, J. Richert et al., Evaporation of light particles from a hot, deformed and rotating nucleus. Nucl. Phys. A **605**, 87–119 (1996). https://doi.org/10.1016/0375-9474(96)00180-7

21. P. Schuurmans, J. Camps, P. De Moor et al., Angular distributions of α particles emitted by deformed oriented nuclei. Phys. Rev. Lett. **82**, 4787–4790 (1999). https://doi.org/10.1103/PhysRevLett.82.4787

22. Y. Jia, J.D. Bao, Calculations of the anisotropy of the fission fragment angular distribution and neutron emission multiplicities prescission from langevin dynamics. Phys. Rev. C **75**, 034601 (2007). https://doi.org/10.1103/PhysRevC.75.034601

23. Z.H. Liu, J.D. Bao, Role of the coupling between neck and radial degrees of freedom in evolution from dinucleus to mononucleus. Phys. Rev. C **83**, 044613 (2011). https://doi.org/10.1103/PhysRevC.83.044613

24. H.F. Zhang, H.F. Zhang, J.Q. Li et al., Spontaneous fission with β-parameterized quasimolecular shape. Phys. Rev. C **90**, 054313 (2014). https://doi.org/10.1103/PhysRevC.90.054313

25. Y. Tanimura, D. Lacroix, S. Ayik, Microscopic phase-space exploration modeling of ^{258}Fm spontaneous fission. Phys. Rev. Lett. **118**, 152501 (2017). https://doi.org/10.1103/PhysRevLett.118.152501

26. H. Tao, J. Zhao, Z.P. Li et al., Microscopic study of induced fission dynamics of ^{226}Th with covariant energy density functionals. Phys. Rev. C **96**, 024319 (2017). https://doi.org/10.1103/PhysRevC.96.024319

27. N. Wang, W. Ye, Probing nuclear dissipation with first-chance fission probability. Phys. Rev. C **97**, 014603 (2018). https://doi.org/10.1103/PhysRevC.97.014603

28. N. Wang, W. Ye, Probing postsaddle dissipation with light-particle multiplicity of hot heavy nuclear systems. Phys. Rev. C **98**, 034614 (2018). https://doi.org/10.1103/PhysRevC.98.034614

29. K. Pomorski, J.M. Blanco, P.V. Kostryukov et al., Fission fragment mass yields of Th to Rf even-even nuclei *. Chin. Phys. C **45**, 054109 (2021). https://doi.org/10.1088/1674-1137/abec69

30. P.V. Kostryukov, A. Dobrowolski, B. Nerlo-Pomorska et al., Potential energy surfaces and fission fragment mass yields of even-even superheavy nuclei *. Chin. Phys. C **45**, 124108 (2021). https://doi.org/10.1088/1674-1137/ac29a3

31. H. Zheng, S. Burrello, M. Colonna et al., Connecting the nuclear equation of state to the interplay between fusion and quasifission processes in low-energy nuclear reactions. Phys. Rev. C **98**, 024622 (2018). https://doi.org/10.1103/PhysRevC.98.024622

32. L. Guo, C.W. Shen, C. Yu et al., Isotopic trends of quasifission and fusion-fission in the reactions ^{48}Ca+^{239,244}Pu. Phys. Rev. C **98**, 064609 (2018). https://doi.org/10.1103/PhysRevC.98.064609

33. C. Gregoire, C. Ngo, E. Tomasi et al., Fast fission phenomenon. Nucl. Phys. A **387**, 37–50 (1982). https://doi.org/10.1016/0375-9474(82)90190-7

34. C. Grégoire, C. Ngô, B. Remaud, Fast fission phenomenon, deep inelastic reactions and compound nucleus formation described within a dynamical macroscopic model. Nucl. Phys. A **383**, 392–420, 024622 (1982). https://doi.org/10.1016/0375-9474(82)90084-7

35. P. Glässel, D.v. Harrach, H.J. Specht, et al., Observation of proximity- and non-equilibrium effects in ternary heavy ion reactions. Z. Phys. A **310**, 189–216 (1983). https://doi.org/10.1007/BF01415224

36. S. Leray, X.S. Chen, G.Y. Fan et al., Investigation of fast fission in the ^{35}Cl+^{238}U system. Nucl. Phys. A **423**, 175–188 (1984). https://doi.org/10.1016/0375-9474(84)90304-X

37. Z. Zheng, B. Borderie, D. Gardes et al., Further experimental evidence for fast fission. Nucl. Phys. A **422**, 447–460 (1984). https://doi.org/10.1016/0375-9474(84)90526-8

38. K. Wen, F. Sakata, Z.X. Li et al., Non-gaussian fluctuations and non-markovian effects in the nuclear fusion process: Langevin dynamics emerging from quantum molecular dynamics simulations. Phys. Rev. Lett. **111**, 012501 (2013). https://doi.org/10.1103/PhysRevLett.111.012501

39. P. Russotto, P.Z. Wu, M. Zoric et al., Symmetry energy from elliptic flow in ^{197}Au+^{197}Au. Phys. Lett. B **697**, 471–476 (2011). https://doi.org/10.1016/j.physletb.2011.02.033

40. C. Rizzo, V. Baran, M. Colonna et al., Symmetry energy effects on fusion cross sections. Phys. Rev. C **83**, 014604 (2011). https://doi.org/10.1103/PhysRevC.83.014604

41. J.L. Tian, X. Li, X.Z. Wu et al., Dynamic potential barrier in the entrance phase of heavy-ion fusion reactions. Eur. Phys. J. A **42**, 105 (2009). https://doi.org/10.1140/epja/i2009-10850-2

42. J.L. Tian, L. Ou, H.J. Hao et al., Dynamical shell effect in the fusion reactions. Int. J. Mod. Phys. E **20**, 1755–1764 (2011). https://doi.org/10.1142/S0218301311019556

43. C. Li, J.L. Tian, Y.J. Qin et al., Determination of the nucleon-nucleon interaction in the ImQMD model by nuclear reactions at the fermi energy region. Chin. Phys. C **37**, 114101 (2013). https://doi.org/10.1088/1674-1137/37/11/114101

44. J.L. Tian, X.Z. Wu, K. Zhao et al., Properties of the composite systems formed in the reactions of ^{238}U+^{238}U and ^{232}Th+^{250}Cf. Phys. Rev. C **77**, 064603 (2008). https://doi.org/10.1103/PhysRevC.77.064603

45. C. Li, J.L. Tian, L. Ou et al., Finite-size effects on fragmentation in heavy-ion collisions. Phys. Rev. C **87**, 064615 (2013). https://doi.org/10.1103/PhysRevC.87.064615

46. N. Wang, J.L. Tian, W. Scheid, Systematics of fusion probability in "hot" fusion reactions. Phys. Rev. C **84**, 061601 (2011). https://doi.org/10.1103/PhysRevC.84.061601

47. P. Goddard, P. Stevenson, A. Rios, Fission dynamics within time-dependent Hartree-Fock: Deformation-induced fission. Phys. Rev. C **92**, 054610 (2015). https://doi.org/10.1103/PhysRevC.92.054610

48. F. Bocage, J. Colin, M. Louvel et al., Dynamical effects in nuclear collisions in the fermi energy range: aligned breakup of heavy projectiles. Nucl. Phys. A **676**, 391–408 (2000). https://doi.org/10.1016/S0375-9474(00)00193-7

49. E.D. Filippo, A. Pagano, E. Piasecki et al., Dynamical fission in ^{124}Sn+^{64}Ni collision at 35A MeV. Phys. Rev. C **71**, 064604 (2005). https://doi.org/10.1103/PhysRevC.71.064604

50. E. De Filippo, A. Pagano, P. Russotto et al., Correlations between emission timescale of fragments and isospin dynamics in ^{124}Sn+^{64}Ni and ^{112}Sn+^{58}Ni reactions at 35A MeV. Phys. Rev. C **86**, 014610 (2012). https://doi.org/10.1103/PhysRevC.86.014610

51. E.V. Pagano, L. Acosta, L. Auditore et al., Statistical against dynamical PLF fission as seen by the IMF-IMF correlation functions and comparisons with CoMD model. Jour. of Phys. Conf. Series **1014**, 012011 (2018). https://doi.org/10.1088/1742-6596/1014/1/012011

52. S. Piantelli, G. Casini, A. Ono et al., Dynamical fission of the quasiprojectile and isospin equilibration for the system ^{80}Kr+^{48}Ca at 35 MeV/nucleon. Phys. Rev. C **101**, 034613 (2020). https://doi.org/10.1103/PhysRevC.101.034613

53. R.S. Wang, Y. Zhang, Z.G. Xiao et al., Time-dependent isospin composition of particles emitted in fission events following ^{40}Ar+^{197}Au at 35 MeV/u. Phys. Rev. C **89**, 064613 (2014). https://doi.org/10.1103/PhysRevC.89.064613

54. G. Casini, P.G. Bizzeti, P.R. Maurenzig et al., Fission time scales from anisotropic in-plane distributions in ^{100}Mo+^{100}Mo and ^{120}Sn+^{120}Sn collisions around 20A MeV. Phys. Rev. Lett. **71**, 2567–2570 (1993). https://doi.org/10.1103/PhysRevLett.71.2567

55. Q.H. Wu, X.Y. Diao, F.H. Guan et al., Transport model studies on the fast fission of the target-like fragments in heavy ion collisions. Phys. Lett. B **797**, 134808 (2019). https://doi.org/10.1016/j.physletb.2019.134808

56. Q.H. Wu, F.H. Guan, X.Y. Diao et al., Symmetry energy effect on emissions of light particles in coincidence with fast fission. Phys. Lett. B **811**, 135865 (2020). https://doi.org/10.1016/j.physletb.2020.135865

57. M. Pancic, Y. Qiang, J.C. Pei et al., Shape evolutions in fission dynamics within time-dependent Hartree-Fock approach. Front. Phys. **8**, 351 (2020). https://doi.org/10.3389/fphy.2020.00351

58. F.H. Guan, X.Y. Diao, Y.J. Wang et al., A Compact Spectrometer for Heavy Ion Experiments in the Fermi energy regime. Nucl. Inst. Meth. A **1011**, 165592 (2021). https://doi.org/10.1016/j.nima.2021.165592

59. Y.J. Wang, F.H. Guan, X.Y. Diao et al., CSHINE for studies of HBT correlation in heavy ion reactions. Nucl. Sci. Tech. **32**, 4 (2021). https://doi.org/10.1007/s41365-020-00842-2

60. F.H. Guan, Y.J. Wang, X.Y. Diao et al., Track recognition for the ΔE-E telescopes with silicon strip detectors. Nucl. Inst. Meth. A **1029**, 166461 (2022). https://doi.org/10.1016/j.nima.2022.166461

61. Y.J. Wang, F.H. Guan, Q.H. Wu et al., The emission order of hydrogen isotopes via correlation functions in 30 MeV/u Ar+Au reactions. Phys. Lett. B **825**, 136856 (2022). https://doi.org/10.1016/j.physletb.2021.136856

62. X.L. Wei, F.H. Guan, H.R. Yang et al., Development of parallel plate avalanche counter for heavy ion collision in radioactive ion beam. Nucl. Eng. Tech. **52**, 575–580 (2020). https://doi.org/10.1016/j.net.2019.08.020

63. G.X. Dai, Y.J. Qi, J.W. Zheng, et al., Fission measurement on 5.5 to 21.7 MeV/A ^{28}Si +^{197}Au system (I) linear momentum transfer and distribution of out-of-reaction plane. High Ene. Phys. Nucl. Phys. **14**, 629–634 (1990)

64. Z.H. Liu, J.C. Xu, H.Q. Zhang et al., Subbarrier complete fusion-fission reactions of ^{16}O+^{232}Th. High Ene. Phys. Nucl. Phys. **18**, 489–495 (1994)

65. V.E. Viola, K. Kwiatkowski, M. Walker, Systematics of fission fragment total kinetic energy release. Phys. Rev. C **31**, 1550–1552 (1985). https://doi.org/10.1103/PhysRevC.31.1550

66. X. Qian, H.Q. Zhang, Z.H. Liu, et al., Fission fragment angular correlation in the reaction induced by 84.0 MeV ^{16}O bombarded ^{238}U. High Ene. Phys. Nucl. Phys. **17**, 173–178 (1993)

67. J.W. Zheng, E.J. Wu, Z.G. Xiao et al., Investigation of fission properties in the reaction 25 MeV/u ^{40}Ar+^{209}Bi. High Ene. Phys. Nucl. Phys. **23**, 409–416 (1999)

68. J. Zheng, E.J. Wu, C. Zhang et al., Measurement of fission time scale and excitation energy at scission for 25 MeV/u ^{40}Ar+^{209}Bi fission reaction. High Ene. Phys. Nucl. Phys. **23**, 946–953 (1999)

69. E.J. Wu, J.W. Zheng, Z.G. Xiao et al., Evidence for different fission behavior of hot nuclei formed in central and peripheral collisions of reaction at 25 MeV/u. Chin. Phys. Lett. **16**, 499, 024622 (1999). https://doi.org/10.1088/0256-307X/16/7/011